

Article

Conceptual Design of an Internally Reinforced Pressure Vessel for Hydrogen Storage in Heavy-Duty Fuel Cell Vehicles

Tinashe Mazarire *, Alexander Galloway and Athanasios Toumpis 

Department of Mechanical & Aerospace Engineering, University of Strathclyde, Glasgow G1 1XJ, UK; alex.galloway@strath.ac.uk (A.G.); athanasios.toumpis@strath.ac.uk (A.T.)

* Correspondence: tinashe.mazarire.2018@uni.strath.ac.uk

Abstract

Current onboard hydrogen storage systems are volumetrically inefficient and represent a major constraint on the driving range of heavy-duty fuel cell vehicles. This work presents a conceptual model of an internally reinforced Type I rectangular-shaped pressure vessel as a solution to enhance the volumetric efficiency of hydrogen storage in heavy-duty vehicles. The pressure vessel's geometry incorporates an internal reinforcing structure to ensure both the structural integrity of the vessel and compliance with the standards for onboard hydrogen storage. Initially, an analytical approach was employed to determine the base parameters of the wall and the internal structure of the reinforced pressure vessel. Finite element analysis was then conducted to validate the analytical solutions and assess the structural integrity of the pressure vessel under design pressure conditions. This was followed by a parametric optimisation study in which the design parameters were systematically varied to identify an optimal pressure vessel design. The 35 MPa reinforced titanium pressure vessel offers 29% more volumetric capacity than the conventional Type IV storage system. The gravimetric capacity of the titanium pressure vessel is low, 2.9 wt%; despite this, the mass of the vessel is applicable in HDVs. This design increases hydrogen storage capacity, offering a range increase of approximately 29% for the same design space.

Keywords: hydrogen storage vessel; fuel cell vehicles; finite element analysis; design space; stress analysis; pressure vessel; titanium alloy; internally reinforced structure; volumetric efficiency

1. Introduction

Hydrogen, as a zero-carbon energy source, exhibits high energy density per mass (120 MJ/kg), surpassing conventional fuels such as diesel, with only 44 MJ/kg [1]. However, at standard temperature and pressure (STP) conditions, hydrogen has low energy density per volume, i.e., 10 MJ/m³ compared to the 34,600 MJ/m³ of diesel [2]. To enhance the volumetric density of hydrogen at STP, the fuel must be stored as compressed gas, cryogenic liquid or in solid materials. This work focuses solely on compressed hydrogen owing to its high performance and favourable practicality in vehicle applications compared to the aforementioned hydrogen storage systems [3–5]. Nonetheless, compressed hydrogen storage systems are notably bulky and demand substantial volumes to store usable amounts of hydrogen in fuel cell electric heavy-duty vehicles (HDVs). For instance, Wrightbus's StreetDeck Hydroliner bus has hydrogen tanks with a total volume of 1.12 m³ to store 27 kg of hydrogen at 35 MPa, enabling a driving range of approximately 280 miles [6].



Academic Editor: Chiara Milanese

Received: 10 January 2026

Revised: 11 February 2026

Accepted: 23 February 2026

Published: 25 February 2026

Copyright: © 2026 by the authors.

Licensee MDPI, Basel, Switzerland.

This article is an open access article distributed under the terms and

conditions of the [Creative Commons](https://creativecommons.org/licenses/by/4.0/)

[Attribution \(CC BY\)](https://creativecommons.org/licenses/by/4.0/) license.

Kast et al. [7,8] and Gangloff et al. [9] conducted assessments of the design spaces available for hydrogen storage on a range of HDV-classes. The studies [7–9] identified various potential mounting locations for hydrogen storage systems on HDVs, such as the rear of the cabin, along the side rail, or on the roof of the vehicle, which all depend on vehicle weight class and use of the vehicle. Most commercially available HDVs favour hydrogen tank installation at the cabin rear or in the rear section of the vehicle due to larger utilisable space in these locations, for example, the Wrightbus StreetDeck Hydroliner [6] and Hyundai XCIENT [10] fuel cell vehicles.

Current fuel cell electric vehicles (FCEVs) utilise Type IV cylindrical pressure vessels for onboard hydrogen storage. These vessels are made of a high-density polyethylene (HDPE) liner wrapped with a carbon fibre composite layer [11,12]. Type IV pressure vessels are distinguished by their superior gravimetric capacity, rendering them an exceptionally lightweight storage solution for onboard applications [5,13,14]. Gravimetric capacity defines the mass of stored hydrogen in relation to the total mass of the hydrogen storage system expressed as a weight percentage (wt%) [15]. However, the cylindrical shape of Type IV pressure vessels results in limited volumetric efficiency within a defined design space, as illustrated in Figure 1.

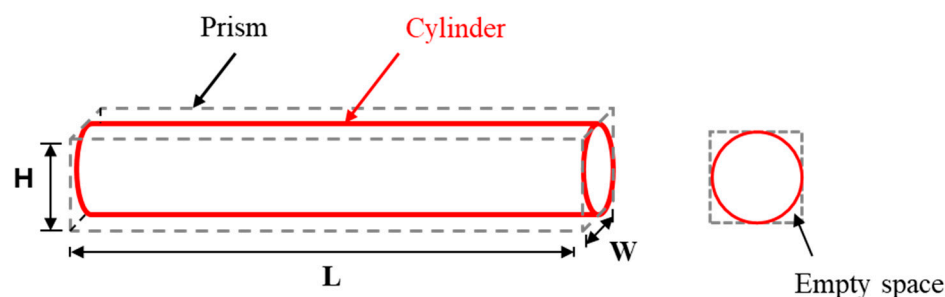


Figure 1. Illustration of prismatic container volume against cylindrical container.

The volumetric efficiency of the cylinder can be derived as follows:

Volume of a prism, V_{prism} :

$$V_{prism} = L \times W \times H \quad (1)$$

Volume of cylinder, $V_{cylinder}$:

$$V_{cylinder} = \pi \left(\frac{W^2}{4} \right) L \quad (2)$$

where L is the length of the rectangular prism, W is the width and H is the height.

Since the volumetric efficiency of a rectangular prism is 1, the volumetric efficiency of a cylindrical vessel can be calculated as

$$\frac{V_{cylinder}}{V_{prism}} = \frac{\pi}{4} = 0.785 \quad (3)$$

The volumetric efficiency calculations of a cylinder shown in Equations (1)–(3) suggest that the implementation of a rectangular pressure vessel offers an approximate 21% increase in hydrogen storage capacity relative to a cylindrical one. Nevertheless, prismatic pressure vessels are unsuitable for high-pressure storage purposes due to high bending stresses in the plates and high stress concentrations along the edges [16]; thus, cylindrical ends are proposed herein.

Öztaş et al. [17] investigated a box-shaped metallic pressure vessel reinforced with tension struts for use in small commercial vehicles. Considering the scalability of such a design for HDV applications, the design would require a significant number of thin struts, which might pose manufacturing challenges. The study [17] employed tooling steel 1.270, a high-strength steel, but highly susceptible to hydrogen embrittlement [18], which may render it unsuitable for high-pressure hydrogen storage applications. The notable high density of this steel grade, 8.05 g/cm^3 , resulted in a hydrogen storage tank with substantial mass, as reported in a subsequent study [19].

Given the complex geometry of a pressure vessel reinforced with an internal structure, wire arc additive manufacturing (WAAM) is particularly well-suited to this application due to its flexibility to manufacture complex shapes [20] and its higher deposition rates compared to other additive manufacturing processes [21]. Additionally, the cost of the filler wire is more economical compared to metal powders required by other methods such as selective laser melting [22,23]. Additive manufacturing has experienced significant growth over the past decade [24], driven by key benefits such as reduced material waste and lower environmental impact compared to conventional manufacturing methods [25,26]. These factors contribute to its potential as a highly sustainable manufacturing approach. Post-processed WAAM components also offer enhanced mechanical properties; for instance, Bermingham et al. [27] demonstrated that a heat-treated β -titanium alloy component produced via WAAM achieved a yield strength of 1600 MPa, which is substantially higher than that of conventional wrought titanium, i.e., 1200 MPa. Thus, due to the high strength to weight ratio offered by this material, it was selected for the present study.

This study extends current work on Type I reinforced pressure vessel design by investigating a novel internally titanium-reinforced pressure vessel for hydrogen storage in HDVs, with a primary focus on buses. The research proposes a prismatic pressure vessel with cylindrical ends to address the volumetric inefficiencies of existing Type IV cylindrical pressure vessels. An internal reinforcement structure is introduced to support the two parallel rectangular plates, thereby reducing bending stresses in the plates. A comparison with the existing Type IV storage system is conducted to evaluate the benefits and drawbacks of the proposed Type I reinforced design.

2. Design Principle of the Internally Reinforced Type I Pressure Vessel

An analytical approach is used to define the pressure vessel's reference geometry based on the principles of force equilibrium equations. First, an analysis of the cylindrical section is conducted to determine the thickness of the pressure vessel. Thin wall membrane stress analysis is used to calculate the wall thickness. The calculated wall thickness is applied throughout the vessel. An analysis of the internal structure follows that determines the cross-sectional area of the internal reinforcement required to withstand the axial force experienced by the internal structure.

ISO 19881 [28] for hydrogen storage in onboard applications is used as the design standard for the pressure vessel introduced in this study. The standard specifies that the pressure vessel design should have a minimum stress ratio of 2.25. Stress ratio is defined as the stress at burst pressure divided by the stress at nominal working pressure [28]. Nominal working pressure is the working pressure as specified by the pressure vessel manufacturer at a uniform gas temperature of $15 \text{ }^\circ\text{C}$ [28]. A conservative design is presented in this study, which assumes that the pressure vessel fails (bursts) when the material's yield strength is reached.

Given that the reinforced pressure vessel design will be subjected to hydrogen during service, it is imperative to account for the mechanical properties of titanium in such conditions. Like most metals, titanium is inherently susceptible to hydrogen embrittle-

ment [29,30]. However, studies [31,32] have reported that the yield strength and ultimate tensile strength of hydrogen-charged specimens either exhibit marginal reductions or, in some cases, slight increases, contingent upon the experimental conditions. Since previous studies have shown that the yield strength of titanium alloys is marginally affected by hydrogen exposure, the yield strength of WAAM-fabricated β -titanium reported by Bermingham et al. [27] tested in the absence of hydrogen is used in this conceptual study. For practical applications, experimental validation under hydrogen exposure would be required.

The dimensions of the pressure vessel are chosen based on a design space of 2500 mm \times 2200 mm \times 500 mm. This reference volume is representative and compatible with a range of HDVs in the UK [33], including buses and 44-tonne heavy goods vehicles. The nominal working pressure for the vessel used in this study is 35 MPa. Figure 2 illustrates the reference geometry of the pressure vessel.

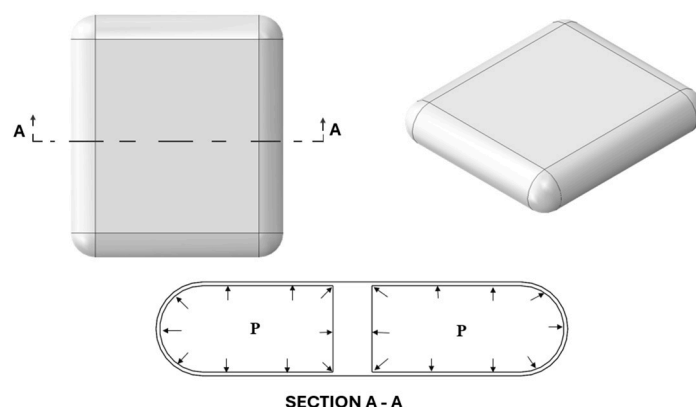


Figure 2. Pressure vessel isometric and cross-sectional view.

2.1. Shell Design

Membrane stress analysis is used to evaluate pressurised cylindrical vessels. The hoop and axial stresses can be determined through static equilibrium conditions [34]. Figure 3 illustrates the loading conditions and stresses acting on a pressurised cylindrical section.

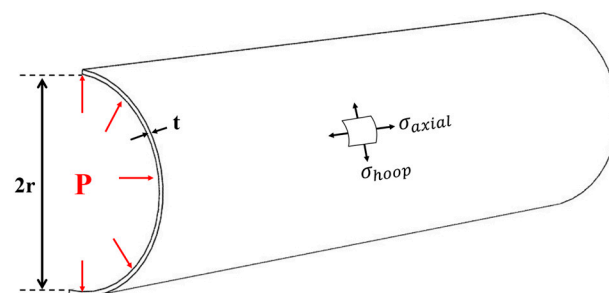


Figure 3. Stresses in a pressurised cylindrical section.

Solving the force equilibrium along the circumferential and radial directions gives:

Hoop stress:

$$\sigma_{hoop} = \frac{pr}{t} \quad (4)$$

Axial stress:

$$\sigma_{axial} = \frac{pr}{2t} \quad (5)$$

where p is the applied internal pressure, r is the radius and t is the thickness of the pressure vessel.

Hoop stress, the highest stress of the two, is used to calculate the wall thickness of the entire pressure vessel.

2.2. Internal Structure Design of the Pressure Vessel

The internal reinforcement acts as a load-bearing structure between the two parallel plates by carrying the tensile load resulting from the pressure acting on these plates. The force equilibrium equation between the pressure acting on the plates and the axial stress in the internal structure is calculated as

$$p(A_{plate}) = \sigma A_{internal\ structure} \quad (6)$$

The cross-sectional area of the internal structure can be calculated by rearranging Equation (6):

$$A_{internal\ structure} = \frac{pA_{plate}}{\sigma} \quad (7)$$

where p is the burst pressure, A_{plate} is the cross-sectional area of the rectangular plate, $A_{internal\ structure}$ is the cross-sectional area of the reinforcing structure and σ is the tensile strength of the material. Equation (7) assumes pure axial stress acting in the internal structure and Figure 4 depicts the stress in the internal structure resulting from the pressure acting on the plates.

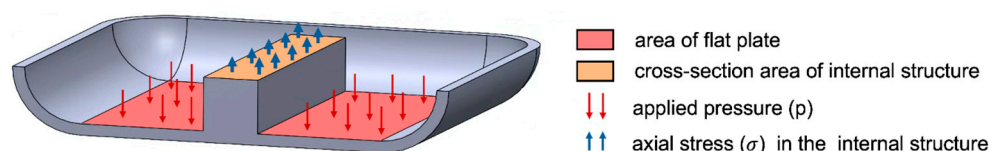


Figure 4. Stress in the internal structure under pressure applied on flat plates.

The value determined by Equation (7) represents the total cross-sectional area of the internal structure within the pressure vessel. Contrary to a single structure, as depicted in Figure 2, the internal structure is modelled as ‘ribs’, each with a thickness of 2 mm. The total cross-sectional area of these 2 mm ribs equates to the calculated cross-sectional area of the internal structure ($A_{internal\ structure}$). Equation (7) will be validated using FEA results in the subsequent sections. Table 1 presents the design parameters for the pressure vessel.

Table 1. Design parameters.

Tank Parameters	Value
Material	β -titanium alloy
Yield strength (MPa)	1600
Poisson’s ratio	0.31
Density (kgm^{-3})	4850
Design space (m)	$2.5 \times 2.2 \times 0.5$
Working pressure (MPa)	35
Design safety factor	2.25

3. Numerical Analysis

Finite element analysis is conducted using ABAQUS Standard software 2021. The material used in this analysis is β -titanium alloy with linear elastic properties and a yield strength of 1600 MPa [27]. For a conservative design, a stress of 1400 MPa is used for both the calculations of shell thickness and rib cross-sectional area, calculated using Equation (4) and Equation (7), respectively. Using the design parameters in Table 1, the radius is approximately $17\times$ higher than the thickness of the pressure vessel; hence, thin wall membrane stress analysis is valid [34]. To expedite the computational analysis, one-eighth of the pressure vessels is modelled using shell elements, as depicted in Figure 5. Shell elements are suitable for modelling both thick and thin models and provide accurate and

robust results [35]. Based on the initial results of the reference geometry, an optimisation study is conducted to enhance the structural integrity of the pressure vessel. Both maximum principal and von Mises stress are considered in the analysis. Since this is an elastic burst pressure analysis and the material is assumed to fail upon reaching the yield stress, the reported stress values in this study correspond to the governing (highest) stress obtained from these metrics.

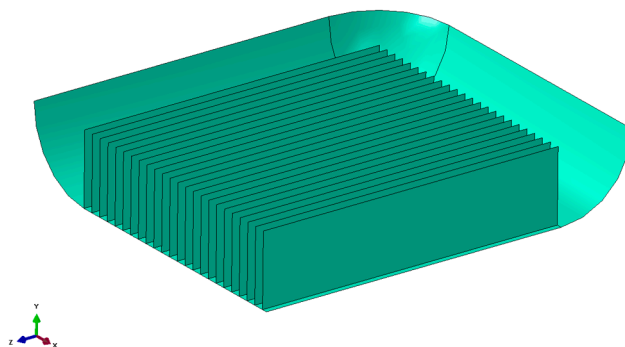


Figure 5. Shell model of the pressure vessel.

3.1. Finite Element Model

The wall and the rib structure are modelled as homogenous shells. The ribs are uniformly spaced along the pressure vessel's rectangular section. An internal pressure load of 78.75 MPa is applied to the interior surfaces of the pressure vessel. This pressure corresponds to 225% of the nominal working pressure of 35 MPa and represents the burst pressure condition used in the analysis. Since only one-eighth of the pressure vessel is modelled for the analysis, symmetry boundary conditions are applied to the edges of the shell model. Each boundary condition corresponds to a specific plane of symmetry along the X, Y, and Z axes within ABAQUS interface. These symmetry boundary conditions are defined by constraining the normal displacement and the corresponding rotational degrees of freedom on each plane of symmetry.

S4R mesh elements with reduced integration are used for the initial numerical analysis, as they offer accurate results while minimising computational cost [35]. To ensure even element distribution along the curved sections of the vessel, curvature control is applied during meshing.

A mesh convergence study is conducted to validate the numerical accuracy of the model. The displacement at a reference node located at the end of the cylindrical section is used as the control metric. The mesh convergence study is of paramount significance in FEA to achieve both accuracy of the numerical analysis and computational efficiency [36]. Mesh convergence is assumed when the difference in maximum displacement relative to a finer mesh is less than 2%, which indicates that the solution has converged. Figure 6 presents the results of the mesh convergence study, showing how displacement stabilises as the element size decreases. The final mesh consists of 74,499 elements and 75,306 nodes, representing a 0.8% difference in maximum displacement compared to the finer mesh.

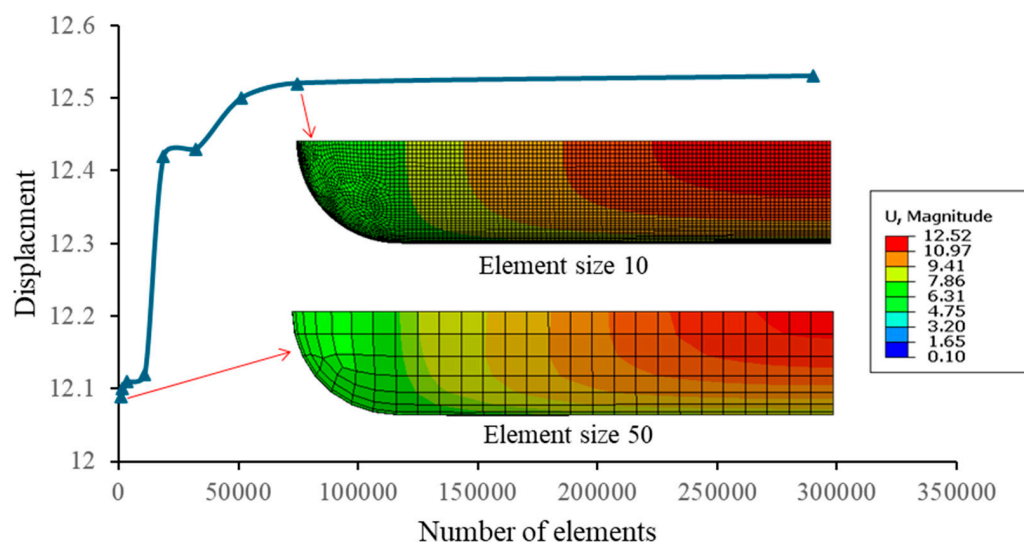


Figure 6. Mesh convergence study.

Initial results from the reference geometry, Figure 7a, indicate that the highest stress is at the juncture between the ribs and the cylindrical wall. This high stress concentration is attributed to the rib's orientation relative to the cylindrical wall. To eliminate this, the design is modified by extending the rib to the cylindrical wall. The results for the redesigned model are depicted in Figure 7b, where the highest maximum principal stress is identified between the first rib and the cylindrical wall.

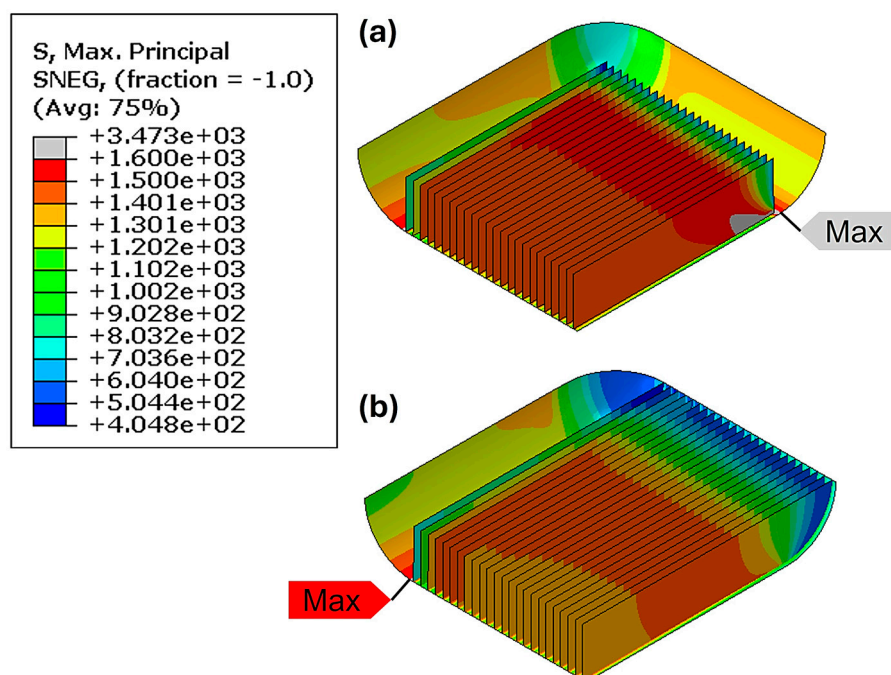


Figure 7. Stress distribution in the shell model: (a) initial model, (b) model with extended rib.

The extended rib creates discrete compartments within the pressure vessel. Consequently, to maintain an interconnected internal space, a hole is introduced through the ribs, which will be discussed in Section 3.4. This ensures that the pressure vessel can be uniformly filled with hydrogen.

3.2. Distance Between the Rib and the Wall

To further examine the stress between the first rib and the cylindrical wall, a 2D planar cross-section of the pressure vessel is considered (Figure 8). A validation study is conducted to ascertain the consistency of results between the planar model and the shell model. A uniform deformation scale factor is applied to the solution to help visualise the vessel's conformity to the applied pressure.

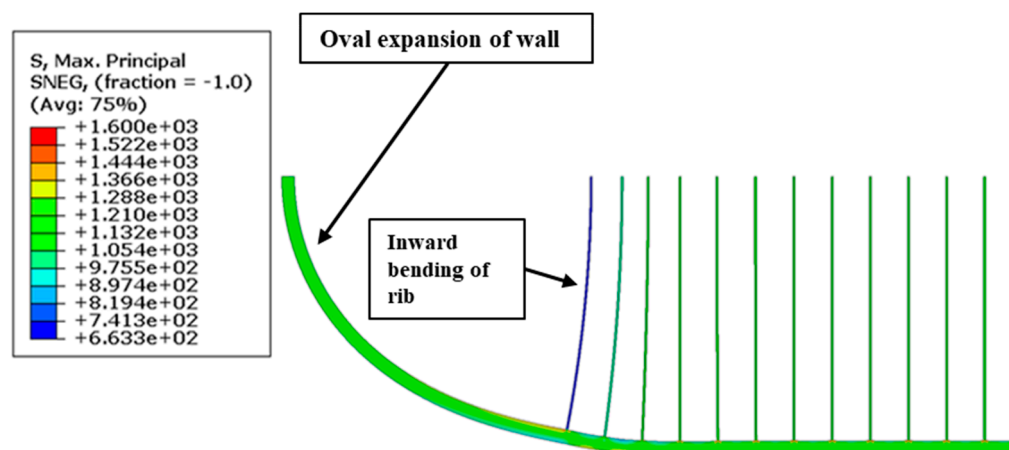


Figure 8. 2D planar cross-sectional view of the pressure vessel.

When the internal pressure is applied, the reinforcing structure constraints the uniform expansion of the cylindrical section. To maintain compatibility of the pressure vessel, the cylindrical section expands in an oval manner. This non-cylindrical expansion leads to an inward bending of the ribs closest to the cylindrical wall, as illustrated in Figure 8. Increasing the distance between the first rib and the shell ensures uniform expansion of the cylindrical section. This also leads to pure tension in the ribs closest to the wall, thereby promoting uniform stress distribution across the ribs.

Figure 9 demonstrates the change in global maximum principal stress as the distance between the shell and the ribs is increased. With the first rib adjacent to the wall, there is a non-uniform expansion of the vessel, which results in high global stress. As the distance between the rib and the wall is increased, the global stress decreases to a minimum. Further increasing the distance leads to more pronounced bending of the wall between the cylindrical section and the first rib, which subsequently leads to an increase in the global principal stress. The optimal distance between the first rib and the cylindrical wall is when the global principal stress is minimal. The resulting maximum principal stress in the rib section, as shown in Figure 9, is 1386 MPa, which closely approximates the 1400 MPa value used in Equation (7) to calculate the cross-sectional area of the rib section.

3.3. Fillet Optimisation

Filletts are imperative for this study due to the stress singularity between the ribs and the wall. The tank's geometry, i.e., the ribs being seven times thinner than the wall, demands an extensive mesh for accurate results. To address this, fillet optimisation is conducted on the planar model from Section 3.2.

The study conducted by Öztas et al. [17] determined that the minimum global stress for a pressure vessel with inner tension struts is reached when the fillets of the struts touch without overlapping, denoted as the critical fillet radius. The critical fillet radius for the current study is inherently limited by the distance between the cylindrical wall and the first rib. Exceeding this radius would result in the fillets overlapping with the cylindrical wall.

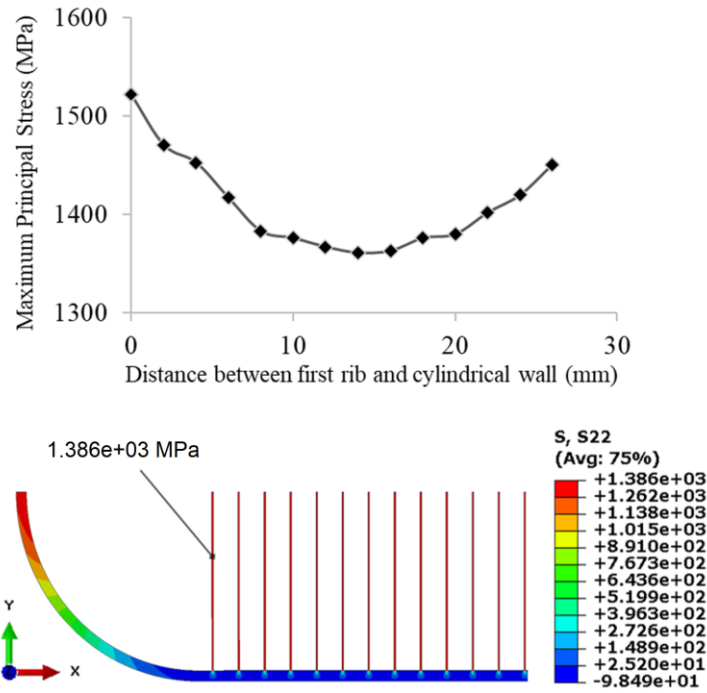


Figure 9. Effect of increasing the distance between the first rib and the cylindrical wall.

For the fillet optimisation study, a triangular mesh with an element size of 5 is utilised. Triangular elements are selected due to the curved geometry of the fillets, as they enable more accurate geometric representation with a relatively coarser mesh. Additionally, they offer greater flexibility for local mesh refinement in regions of geometric or stress complexity [35]. The results of the analysis using the initial mesh are presented in Figure 10a. This mesh consists of 8394 elements and 6440 nodes.

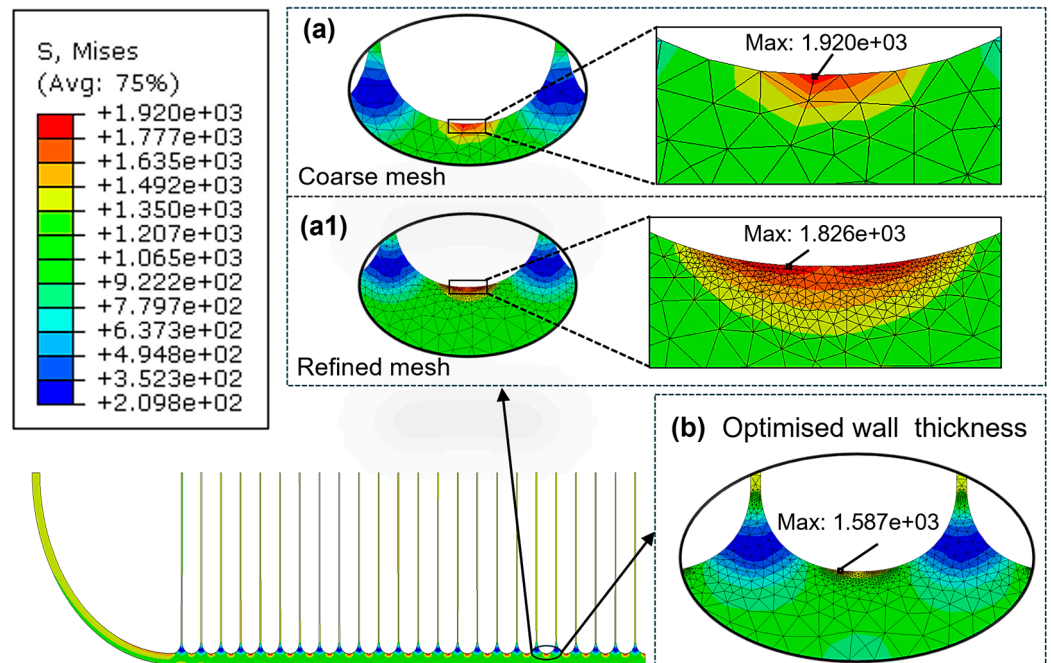


Figure 10. Stress concentration at the tip of each fillet: (a) critical radius with coarse mesh; (a1) refined mesh of (a); (b) after optimisation by increasing wall thickness.

Stress concentrations are observed at the fillet tip; however, the initial mesh resolution (Figure 10a) is insufficient to capture the peak stresses accurately. To address this, localised

mesh refinement using curvature control is performed in the critical region. Figure 10(a1) displays the refined triangular mesh, which provides enhanced resolution around the fillet and captures the stress distribution with greater accuracy. The refined mesh comprises 40,285 elements and 25,281 nodes. The use of smaller elements in high-stress regions enables a more accurate representation of stress gradients, which is essential for evaluating structural integrity in the presence of stress concentrations. The refined mesh analysis indicates that the highest stress does not occur directly on the fillet but rather at the tip of each fillet. This stress concentration is primarily due to the bending of the wall between two adjacent ribs.

To address the bending, an optimisation study is initiated, focusing on increasing the wall thickness. The refined mesh model presented in Figure 10a was used for the thickness optimisation study. The results of this study are presented in Figure 11, which illustrates a decrease in global principal stress as the thickness of the wall is increased. The resulting stress at the fillets, after wall thickness optimisation, is shown in Figure 10b.

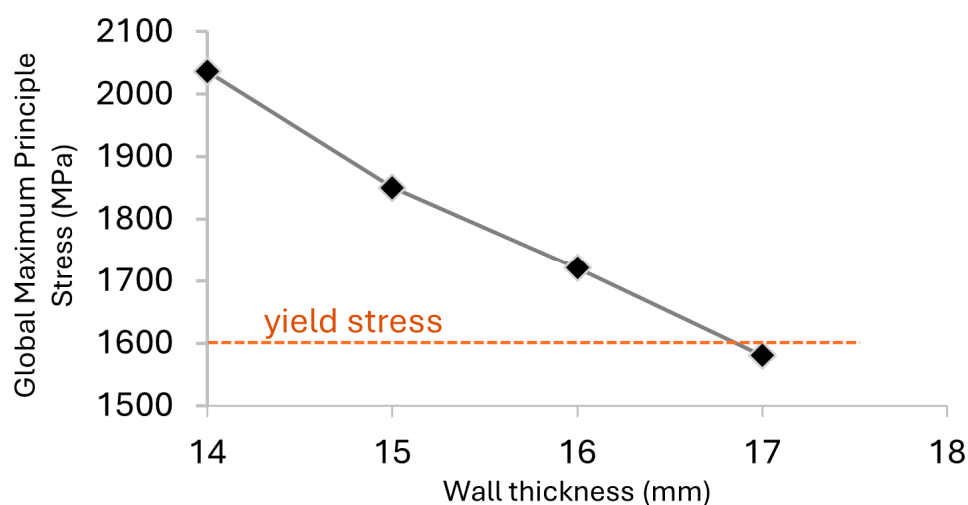


Figure 11. Effect of increasing wall thickness on the global principal stress.

3.4. Optimisation of Rib Hole and Inlet Opening

The objective of the hole optimisation study is to determine the maximum permissible hole diameter, which maximises internal volume and reduces overall mass, thus enhancing the pressure vessel's gravimetric capacity. The optimisation is carried out by introducing holes in the rib section with the lowest stress, i.e., closest to the cylindrical wall and adjacent to the rib fillets. An initial 5 mm radius hole is applied and incrementally increased in steps of 5 mm until the global principal stress reaches the yield stress of the material.

In addition to rib holes, an inlet opening for filling and discharging the pressure vessel is applied on one of the quarter-spherical corners. The dimensions of the inlet opening are adopted from the design reported by Bouhala et al. [37]. A mesh convergence study was conducted for each optimisation iteration. Figure 12 presents the resulting stress distribution in the inlet hole and rib hole.

3.5. Final Design

Figure 13 presents the results of the mesh convergence study and the final stress distribution in the optimised pressure vessel. Tetrahedral elements were selected due to the complex and irregular geometry of the pressure vessel. The reinforced titanium pressure vessel has a mass of 1658 kg and an empty volume capacity of 2.1 m³. Table 2 presents the physical properties of the proposed titanium pressure vessel. The gravimetric capacity,

expressed as weight percentage (wt%), quantifies the mass of the stored hydrogen relative to the total mass of the storage system. It is defined as

$$\text{Gravimetric capacity (wt\%)} = \frac{m_{\text{hydrogen}}}{m_{\text{tank}} + m_{\text{hydrogen}}} \times 100 \tag{8}$$

where m_{hydrogen} denotes the mass of hydrogen that can be stored in the pressure vessel at the specified pressure and m_{tank} represents the mass of the hydrogen storage vessel.

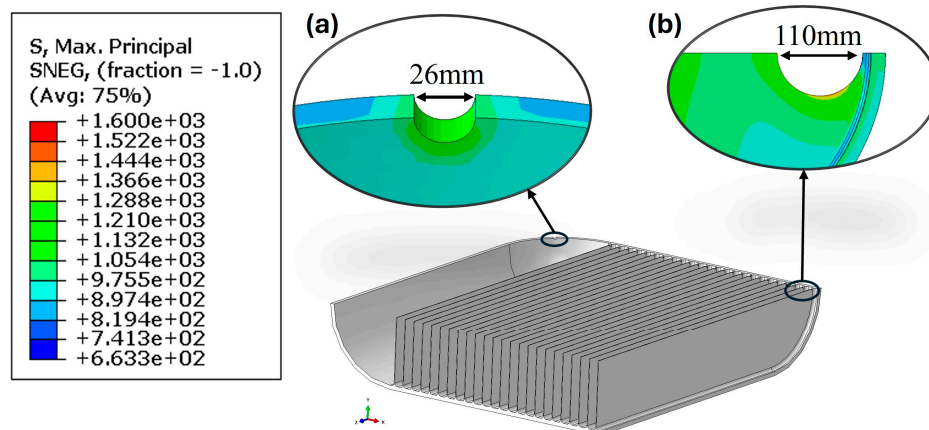


Figure 12. Stress results for the (a) inlet hole and (b) optimised rib hole.

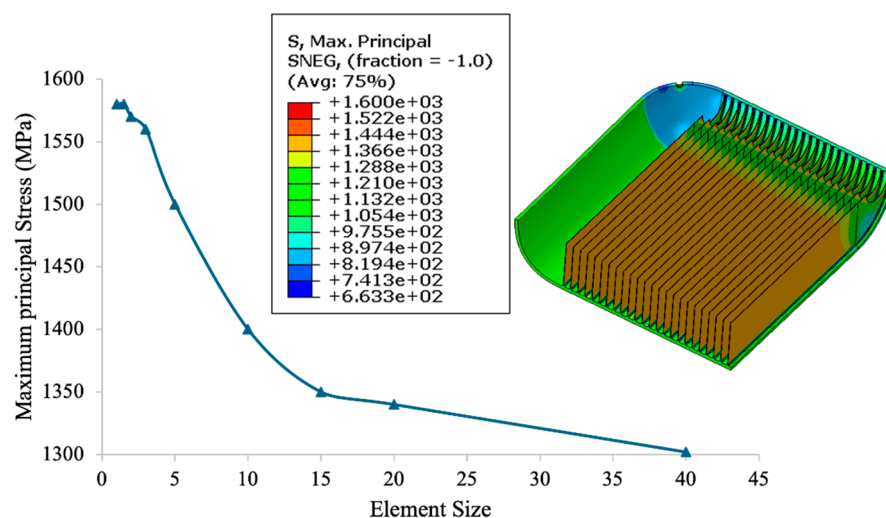


Figure 13. Mesh convergence study results and stress distribution in the optimised model.

Table 2. Reinforced titanium pressure vessel properties.

Property	Value
Mass of empty pressure vessel (kg)	1658
Volume of H ₂ (m ³)	2.1
Mass of H ₂ (kg) ^a	49
Gravimetric capacity (wt%)	2.9
Range (miles) ^b	544

^a Density of hydrogen at 35 MPa is ~23.33 kgm⁻³ [38], ^b Calculated based on 11.1 miles/kg fuel consumption [8].

Equation (8) describes the mass efficiency of the pressure vessel, with a higher gravimetric capacity indicating a more mass-efficient storage system.

4. Discussion

The storage system volumetric capacity of the Type I reinforced titanium pressure vessel is calculated as 19.8 g-H₂/L. This metric is defined as the mass of hydrogen (g) per unit volume (L) occupied by the pressure vessel storage system [39], expressed as

$$\text{Storage system volumetric capacity} = \frac{\text{mass of hydrogen (g)}}{\text{volume of pressure vessel (L)}} \quad (9)$$

The volume of the reinforced pressure vessel design, 2.475 m³, is obtained from the property evaluation tool in ABAQUS. In contrast, Hua et al. [40] reported a volumetric capacity of 17.6 g-H₂/L for a Type IV 35 MPa pressure vessel. This indicates that the reinforced titanium vessel offers a higher hydrogen storage capacity compared to the Type IV vessel design.

Equations (1)–(3) show that cylindrical pressure vessels inherently exhibit a limited volumetric efficiency of ~78.5% within a defined design space, with 100% efficiency representing the ideal case of a rectangular shape. The proposed reinforced titanium pressure vessel has a volumetric efficiency of 90% due to the imposed cylindrical ends. Using this value, the storage system volumetric capacity of the reinforced titanium pressure vessel relative to the design volume (2.75 m³) is 17.8 g-H₂/L.

To evaluate the system volumetric capacity of Type IV pressure vessel within the design space, both the mass of stored hydrogen and volume it occupies must be considered. Based on the dimensions of the design space and the calculated volumetric efficiency of 78.5%, the effective volume occupied by the Type IV storage system is approximately 2.16 m³. Using Equation (9), and a value of 17.6 g-H₂/L, the corresponding mass of hydrogen is 38 kg. This results in a storage system volumetric capacity of ~13.8 g-H₂/L relative to the design space. Hence, utilising the proposed reinforced pressure vessel design yields a 29% increase in hydrogen capacity. This hydrogen capacity enhancement extends the range of a vehicle by approx. 122 miles over the Type IV system for the investigated design space. The range calculation does not explicitly account for the impact of the container weight; rather, it provides a baseline comparison using fuel consumption data for the same vehicle class, as reported by Kast et al. [8]. Table 3 details a comparison between the reinforced pressure vessel design and the 35 MPa Type IV storage system.

Table 3. Hydrogen storage properties of the reinforced titanium and Type IV vessels.

	Titanium	Type IV ^a
Mass of empty pressure vessel (kg)	1658	659
Volume occupied by vessel (m ³)	2.475	2.16
Volume of H ₂ (m ³)	2.1	1.63
Mass of H ₂ (kg)	49	38
Volumetric capacity (g-H ₂ /L)	17.6	13.8
Gravimetric capacity (wt%)	2.9	5.5
Range (miles) ^b	544	422

^a Properties are calculated using a 35 MPa Type IV base model by Hua et al. [40], ^b Calculated based on 11.1 miles/kg fuel consumption [8].

The primary limitation of Type I pressure vessels in vehicular applications is their low gravimetric capacity [5,41]. Table 3 shows a gravimetric capacity of 2.9 wt% for titanium; in comparison, Type IV pressure vessels exhibit a gravimetric capacity of approx. 5.5 wt%, which is consistent with the gravimetric capacity of Type IV pressure vessels reported in the literature [38,39] at 35 MPa. Consequently, the mass of the reinforced pressure vessel is nearly twice as high compared to the current Type IV pressure vessel

system. To contextualise the mass of the Type I reinforced storage system, battery electric vehicles (BEVs), the counterpart solution to decarbonise the transport industry [42,43], are also considered.

Table 4 provides an overview of the properties of batteries for various battery electric buses. The mass of the battery is calculated using the specific energy density of the battery type and capacity, as reported by the corresponding bus manufacturer. Table 4 shows that the batteries used in BEV buses weigh approximately 2 tonnes and their capacity only allows for a driving range between 160 and 200 miles.

Table 4. Overview of battery specifications in selected commercial buses.

Bus Company	Battery Type	Specific Energy Density of Battery (Wh/kg) [44]	Battery Capacity (kWh)	Vehicle Range (miles)	Mass of Battery (kg)
Mercedes Benz eCitaro [45]	Lithium Nickel Manganese Cobalt Oxide (NMC)	~150–250	588	174	~2352
BYD Alexander Dennis Enviro200EV [46]	Lithium Iron Phosphate (LFP)	~80–150	348	160	~2320
Wrightbus Electroliner [47]	NMC	~150–250	454	200	~1816

To compare the energy storage systems of BEV buses to the proposed Type I reinforced pressure vessel design, the differences in their powertrains must be considered. Figure 14 depicts the powertrain configuration of both FCEVs and BEVs. Assuming identical electric motor outputs, FCEVs have additional mass due to the fuel cell and hydrogen storage system. In FCEVs, the battery is smaller, serving primarily to support fuel cell start-up, capture regenerative braking energy, and provide supplementary power during acceleration [48], rather than acting as the main power source.

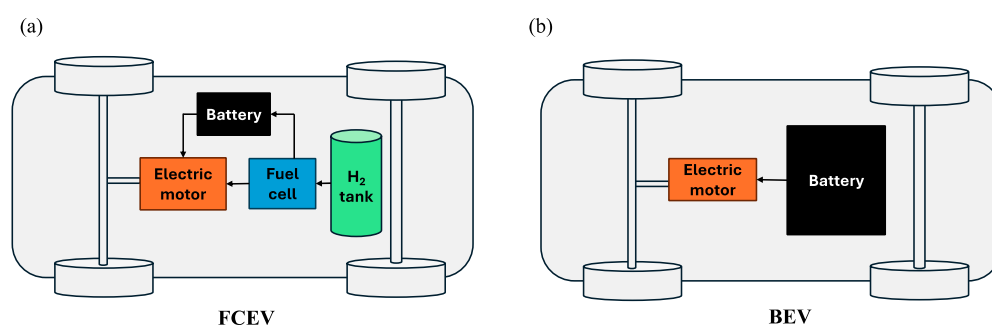


Figure 14. Powertrain schematic: (a) FCEV, (b) BEV.

Table 5 presents the capacity specifications for the battery and the fuel cell system used in the Wrightbus StreetDeck Hydroliner model [6]. The battery type utilised in this model is Lithium Titanate Oxide (LTO), with an energy density ranging from 72 to 99 Wh/kg [49].

Table 5. Capacity and mass of fuel cell module and LTO battery.

	Capacity	Mass
Fuel cell module	85 kW	256 kg
Battery (LTO)	27.4 kWh	~277 kg

The fuel cell module and battery of the FCEV bus weigh an additional 533 kg, bringing the total mass of the titanium storage system to 2191 kg. In contrast to the battery mass in buses presented in Table 4, the titanium-reinforced pressure vessels offer a substantially higher driving range, 544 miles, compared to battery electric buses. This comparison highlights that the mass of the proposed pressure vessel design is not a primary concern, as such mass is applicable in HDVs.

5. Conclusions

This research work demonstrated a viable conceptual solution to enhance hydrogen storage capacity in HDVs through optimised utilisation of the available design space. Type IV cylindrical pressure vessels have limited volumetric efficiency with respect to the design space, limiting the hydrogen storage capacity in HDVs. This study presented the design of a volumetrically efficient Type I internally titanium-reinforced pressure vessel operating at a nominal pressure of 35 MPa for application in fuel cell HDVs. The design process was initiated with an analytical approach to define the base geometry of the pressure vessel, followed by a similar approach for the internal reinforcing structure. Finite element analysis was subsequently conducted to validate the analytical solutions and to assess and optimise the structural integrity of the reference geometry. The proposed design was compared to the existing Type IV cylindrical pressure vessel storage system.

The results demonstrate that the reinforced pressure vessel design offers 29% higher hydrogen capacity, translating to approximately 29% longer driving range for the considered 2.5 m × 2.2 m × 0.5 m design space. The gravimetric capacity of the Type I reinforced design, 2.9 wt%, is lower compared to 5.5 wt% for the conventional Type IV vessel, resulting in a higher mass of 1658 kg versus 659 kg. However, a comparative analysis with BEVs revealed that higher weight and lower range (2352 kg, 174 miles) of the energy storage system is commercially viable. This suggests that the weight of the titanium-reinforced design (1658 kg), providing a driving range of 544 miles, is not a prohibitive factor, despite the lower gravimetric capacity. Therefore, the proposed design offers a feasible alternative for hydrogen storage in HDVs, providing longer range than the current Type IV pressure vessel systems.

Nonetheless, the proposed vessel design presents several limitations that warrant further investigation. These include hydrogen embrittlement during long-term exposure of titanium to high-pressure hydrogen, as well as manufacturing challenges such as residual stresses and geometric distortions associated with WAAM. Areas of high stress may be problematic under cyclic pressure loading during filling and discharging of the pressure vessel or during vehicle-induced vibrations. Future work should therefore focus on experimental validation of the proposed design, alongside a comparative cost and life-cycle assessment with existing Type IV storage systems to evaluate its practical competitiveness.

Despite the identified challenges, the proposed reinforced pressure vessel represents a promising solution for hydrogen storage in HDV. This advancement opens up new opportunities for applications where efficient utilisation of constrained design space and extended range are critical. The demonstrated 29% increase in volumetric efficiency highlights the benefit of improved design space utilisation and may also be relevant to other sectors, such as aviation. Overall, this work lays the groundwork for continued exploration and development of the proposed concept.

Author Contributions: Conceptualization, T.M.; methodology, T.M.; investigation, T.M.; writing—original draft preparation, T.M.; writing—review and editing, T.M., A.G. and A.T.; visualisation, T.M.; supervision, A.G. and A.T. All authors have read and agreed to the published version of the manuscript.

Funding: This research received no external funding.

Data Availability Statement: The original contributions presented in this study are included in the article. Further enquiries can be directed at the corresponding author.

Conflicts of Interest: The authors declare no conflicts of interest.

References

1. Hwang, H.T.; Varma, A. Hydrogen storage for fuel cell vehicles. *Curr. Opin. Chem. Eng.* **2014**, *5*, 42–48. [CrossRef]
2. Mazloomi, K.; Gomes, C. Hydrogen as an energy carrier: Prospects and challenges. *Renew. Sustain. Energy Rev.* **2012**, *16*, 3024–3033. [CrossRef]
3. Usman, M.R. Hydrogen storage methods: Review and current status. *Renew. Sustain. Energy Rev.* **2022**, *167*, 112743. [CrossRef]
4. Maceiras, R.; Alfonsin, V.; Feijoo, J.; Perez-Rial, L.; Lopez-Granados, A. Multi-Criteria Evaluation of Hydrogen Storage Technologies Using AHP and TOPSIS Methodologies. *Hydrogen* **2025**, *6*, 111. [CrossRef]
5. Zheng, J.; Liu, X.; Xu, P.; Liu, P.; Zhao, Y.; Yang, J. Development of high pressure gaseous hydrogen storage technologies. *Int. J. Hydrogen Energy* **2012**, *37*, 1048–1057. [CrossRef]
6. Wrightbus. Wrightbus First Hydrogen Fuel Cell Bus. 2023. Available online: <https://wrightbus.com/en-gb/hydrogen-bus-streetdeck-hydrolinerFCEV> (accessed on 15 July 2024).
7. Kast, J.; Morrison, G.; Gangloff, J.J.; Vijayagopal, R.; Marcinkoski, J. Designing hydrogen fuel cell electric trucks in a diverse medium and heavy duty market. *Res. Transp. Econ.* **2018**, *70*, 139–147. [CrossRef]
8. Kast, J.; Vijayagopal, R.; Gangloff, J.J.; Marcinkoski, J. Clean commercial transportation: Medium and heavy duty fuel cell electric trucks. *Int. J. Hydrogen Energy* **2017**, *42*, 4508–4517. [CrossRef]
9. Gangloff, J.J.; Kast, J.; Morrison, G.; Marcinkoski, J. Design Space Assessment of Hydrogen Storage Onboard Medium and Heavy Duty Fuel Cell Electric Trucks. *J. Electrochem. Energy Convers. Storage* **2017**, *14*, 021001. [CrossRef]
10. Hyundai. XCIENT Fuel Cell Truck. Available online: <https://ecv.hyundai.com/global/en/products/xcient-fuel-cell-truck-fcev/> (accessed on 6 May 2024).
11. Abdalla, A.M.; Hossain, S.; Nisfindy, O.B.; Azad, A.T.; Dawood, M.; Azad, A.K. Hydrogen production, storage, transportation and key challenges with applications: A review. *Energy Convers. Manag.* **2018**, *165*, 602–627. [CrossRef]
12. Okonkwo, P.C.; Barhoumi, E.M.; Belgacem, I.B.; Mansir, I.B.; Aliyu, M.; Emori, W.; Uzoma, P.C.; Beitelmal, W.H.; Akyüz, E.; Radwan, A.B.; et al. A focused review of the hydrogen storage tank embrittlement mechanism process. *Int. J. Hydrogen Energy* **2023**, *48*, 12935–12948. [CrossRef]
13. Hassan, I.A.; Ramadan, H.S.; Saleh, M.A.; Hissel, D. Hydrogen storage technologies for stationary and mobile applications: Review, analysis and perspectives. *Renew. Sustain. Energy Rev.* **2021**, *149*, 111311. [CrossRef]
14. Piraino, F.; Pagnotta, L.; Corigliano, O.; Genovese, M.; Fragiaco, P. Advances in Type IV Tanks for Safe Hydrogen Storage: Materials, Technologies and Challenges. *Hydrogen* **2025**, *6*, 80. [CrossRef]
15. Prewitz, M.; Bardenhagen, A.; Beck, R. Hydrogen as the fuel of the future in aircrafts—Challenges and opportunities. *Int. J. Hydrogen Energy* **2020**, *45*, 25378–25385. [CrossRef]
16. Lee, J.; Choi, Y.; Jo, C.; Chang, D. Design of a prismatic pressure vessel: An engineering solution for non-stiffened-type vessels. *Ocean Eng.* **2017**, *142*, 639–649. [CrossRef]
17. Öztas, K.A.; Weerts, R.A.J.; Ruf, M.G. An analytical and numerical approach to design a type I box-shaped pressure vessel with inner tension struts. *Int. J. Press. Vessel. Pip.* **2021**, *192*, 104441. [CrossRef]
18. Dwivedi, S.K.; Vishwakarma, M. Hydrogen embrittlement in different materials: A review. *Int. J. Hydrogen Energy* **2018**, *43*, 21603–21616. [CrossRef]
19. Öztas, K.A.; Kunze, K.; Jois, K.; Sackmann, J.; Zaremba, S.; Ruf, M.G. A numerical approach to design a type II box-shaped pressure vessel with inner tension struts. *Int. J. Hydrogen Energy* **2022**, *47*, 3927–3938. [CrossRef]
20. Venturini, G.; Montevecchi, F.; Scippa, A.; Campatelli, G. Optimization of WAAM Deposition Patterns for T-crossing Features. *Procedia CIRP* **2016**, *55*, 95–100. [CrossRef]
21. Taberero, I.; Paskual, A.; Álvarez, P.; Suárez, A. Study on Arc Welding Processes for High Deposition Rate Additive Manufacturing. *Procedia CIRP* **2018**, *68*, 358–362. [CrossRef]
22. Jafari, D.; Vaneker, T.H.J.; Gibson, I. Wire and arc additive manufacturing: Opportunities and challenges to control the quality and accuracy of manufactured parts. *Mater. Des.* **2021**, *202*, 109471. [CrossRef]

23. Liberini, M.; Astarita, A.; Campatelli, G.; Scippa, A.; Montevicchi, F.; Venturini, G.; Durante, M.; Boccarusso, L.; Minutolo, F.M.C.; Squillace, A. Selection of Optimal Process Parameters for Wire Arc Additive Manufacturing. *Procedia CIRP* **2017**, *62*, 470–474. [[CrossRef](#)]
24. Altıparmak, S.C.; Xiao, B. A market assessment of additive manufacturing potential for the aerospace industry. *J. Manuf. Process.* **2021**, *68*, 728–738. [[CrossRef](#)]
25. Sword, J.I.; Galloway, A.; Toumpis, A. An environmental impact comparison between wire + arc additive manufacture and forging for the production of a titanium component. *Sustain. Mater. Technol.* **2023**, *36*, e00600. [[CrossRef](#)]
26. Sword, J.I.; Galloway, A.; Toumpis, A. Analysis of Environmental Impact and Mechanical Properties of Inconel 625 Produced Using Wire Arc Additive Manufacturing. *Sustainability* **2024**, *16*, 4178. [[CrossRef](#)]
27. Birmingham, M.J.; Kent, D.; Pace, B.; Cairney, J.M.; Dargusch, M.S. High strength heat-treatable β -titanium alloy for additive manufacturing. *Mater. Sci. Eng. A* **2020**, *791*, 139646. [[CrossRef](#)]
28. ISO 19881:2018; Gaseous Hydrogen—Land Vehicle Fuel Containers. ISO: Geneva, Switzerland, 2018.
29. Navi, N.U.; Tenenbaum, J.; Sabatani, E.; Kimmel, G.; David, R.B.; Rosen, B.A.; Barkay, Z.; Ezersky, V.; Tiferet, E.; Ganor, Y.I.; et al. Hydrogen effects on electrochemically charged additive manufactured by electron beam melting (EBM) and wrought Ti–6Al–4V alloys. *Int. J. Hydrogen Energy* **2020**, *45*, 25523–25540. [[CrossRef](#)]
30. Yao, J.; Tan, Q.; Venezuela, J.; Atrens, A.; Zhang, M.X. Recent research progress in hydrogen embrittlement of additively manufactured metals—A review. *Curr. Opin. Solid State Mater. Sci.* **2023**, *27*, 101106. [[CrossRef](#)]
31. Deconinck, L.; Vidaller, M.T.V.; Quejido, E.B.; Jäggle, E.A.; Depover, T.; Verbeken, K. In-situ hydrogen embrittlement evaluation of as-built and heat treated laser powder bed fused Ti-6Al-4V versus conventionally cold rolled Ti-6Al-4V. *Addit. Manuf.* **2023**, *76*, 103768. [[CrossRef](#)]
32. Nguyen, T.D.; Ansari, N.; Lee, K.H.; Lee, D.H.; Han, J.H.; Lee, S.Y. Effect of Strain Rate on Hydrogen Embrittlement of Ti6Al4V Alloy. *Materials* **2024**, *17*, 1100. [[CrossRef](#)] [[PubMed](#)]
33. The Road Vehicles (Construction and Use) Regulations 1986. Legislation.gov.uk. 2022. Available online: <https://www.legislation.gov.uk/uksi/1986/1078/part/II/chapter/A> (accessed on 11 February 2026).
34. Nash, D.; Aklil, D.; Johnson, E.; Gazey, R.; Ortisi, V. Hydrogen Storage: Compressed Gas. In *Comprehensive Renewable Energy*; Elsevier: Geneva, Switzerland, 2012; pp. 131–155. [[CrossRef](#)]
35. Hibbitt, Karlsson, and Sorensen. *ABAQUS/Standard: User's Manual*; Hibbitt, Karlsson & Sorensen: Pawtucket, RI, USA, 1997; Volume 1.
36. Vu, D.H. Developing Python scripting for mesh convergence in Abaqus. *J. Sci. Tech.-Sect. Spec. Constr. Eng.* **2022**, *5*, 22–31. [[CrossRef](#)]
37. Bouhala, L.; Koutsawa, Y.; Karatrantos, A.; Bayreuther, C. Design of Type-IV Composite Pressure Vessel Based on Comparative Analysis of Numerical Methods for Modeling Type-III Vessels. *J. Compos. Sci.* **2024**, *8*, 40. [[CrossRef](#)]
38. Folkson, R. Hydrogen as an energy vector for transportation vehicles. In *Alternative Fuels and Advanced Vehicle Technologies for Improved Environmental Performance: Towards Zero Carbon Transportation*; Woodhead Publishing: Cambridge, UK, 2022; pp. 151–171. [[CrossRef](#)]
39. Office of Energy Efficiency & Renewable Energy. DOE Technical Targets for Hydrogen Storage Systems for Material Handling Equipment. Available online: <https://www.energy.gov/eere/fuelcells/doe-technical-targets-hydrogen-storage-systems-material-handling-equipment> (accessed on 7 October 2024).
40. Hua, T.Q.; Ahluwalia, R.K.; Peng, J.K.; Kromer, M.; Lasher, S.; McKenney, K.; Law, K.; Sinha, J. Technical assessment of compressed hydrogen storage tank systems for automotive applications. *Int. J. Hydrogen Energy* **2011**, *36*, 3037–3049. [[CrossRef](#)]
41. Barthelemy, H.; Weber, M.; Barbier, F. Hydrogen storage: Recent improvements and industrial perspectives. *Int. J. Hydrogen Energy* **2017**, *42*, 7254–7262. [[CrossRef](#)]
42. Liu, W.; Placke, T.; Chau, K.T. Overview of batteries and battery management for electric vehicles. *Energy Rep.* **2022**, *8*, 4058–4084. [[CrossRef](#)]
43. Iqbal, M.; Benmouna, A.; Becherif, M.; Mekhilef, S. Survey on Battery Technologies and Modeling Methods for Electric Vehicles. *Batteries* **2023**, *9*, 185. [[CrossRef](#)]
44. Walvekar, H.; Beltran, H.; Sripad, S.; Pecht, M. Implications of the Electric Vehicle Manufacturers' Decision to Mass Adopt Lithium-Iron Phosphate Batteries. *IEEE Access* **2022**, *10*, 63834–63843. [[CrossRef](#)]
45. Mercedes Benz. eCitaro Battery Technology. Available online: https://www.mercedes-benz-bus.com/en_GB/models/ecitaro/technology/battery-technology.html (accessed on 15 July 2024).
46. Alexander Dennis. Alexander Dennis BYD. Available online: <https://www.alexander-dennis.com> (accessed on 15 July 2024).
47. Wrightbus. Streetdeck Electroliner BEV. Available online: <https://wrightbus.com/en-gb/electric-bus-streetdeck-electrolinerBEV> (accessed on 15 July 2024).

48. Cunanan, C.; Tran, M.K.; Lee, Y.; Kwok, S.; Leung, V.; Fowler, M. A Review of Heavy-Duty Vehicle Powertrain Technologies: Diesel Engine Vehicles, Battery Electric Vehicles, and Hydrogen Fuel Cell Electric Vehicles. *Clean Technol.* **2021**, *3*, 474–489. [[CrossRef](#)]
49. Nemeth, T.; Schröder, P.; Kuipers, M.; Sauer, D.U. Lithium titanate oxide battery cells for high-power automotive applications—Electro-thermal properties, aging behavior and cost considerations. *J. Energy Storage* **2020**, *31*, 101656. [[CrossRef](#)]

Disclaimer/Publisher’s Note: The statements, opinions and data contained in all publications are solely those of the individual author(s) and contributor(s) and not of MDPI and/or the editor(s). MDPI and/or the editor(s) disclaim responsibility for any injury to people or property resulting from any ideas, methods, instructions or products referred to in the content.